Monthly Notices
of the
ROYAL ASTRONOMICAL SOCIETY

MNRAS **463,** 1534–1542 (2016)
Advance Access publication 2016 August 19

doi:10.1093/mnras/stw2089

A $\mathcal{M} \gtrsim 3$ shock in 'El Gordo' cluster and the origin of the radio relic

A. Botteon,[1,2]★ F. Gastaldello,[3] G. Brunetti[2] and R. Kale[4]

[1]*Dipartimento di Fisica e Astronomia, Università di Bologna, via C. Ranzani 1, I-40127 Bologna, Italy*
[2]*INAF - IRA, via P. Gobetti 101, I-40129 Bologna, Italy*
[3]*INAF - IASF Milano, via E. Bassini 15, I-20133 Milano, Italy*
[4]*National Centre for Radio Astrophysics, Tata Institute of Fundamental Research, Pune 411007, India*

Accepted 2016 August 17. Received 2016 August 8; in original form 2016 June 21

ABSTRACT

We present an X-ray and radio study of the famous 'El Gordo', a massive and distant ($z = 0.87$) galaxy cluster. In the deep (340 ks) *Chandra* observation, the cluster appears with an elongated and cometary morphology, a sign of its current merging state. The GMRT radio observations at 610 MHz confirm the presence of a radio halo, which remarkably overlaps the X-ray cluster emission and connects a couple of radio relics. We detect a strong shock ($\mathcal{M} \gtrsim 3$) in the NW periphery of the cluster, co-spatially located with the radio relic. This is the most distant ($z = 0.87$) and one of the strongest shocks detected in a galaxy cluster. This work supports the relic–shock connection and allows us to investigate the origin of these radio sources in an uncommon regime of $\mathcal{M} \gtrsim 3$. For this particular case we found that shock acceleration from the thermal pool is still a viable possibility.

Key words: radiation mechanisms: non-thermal – shock waves – galaxies: clusters: individual: ACT-CL J0102–4915 – radio continuum: general – X-rays: galaxies: clusters.

1 INTRODUCTION

Galaxy clusters are the largest virialized structures in the Universe and form via aggregation of less massive systems (e.g. Press & Schechter 1974). During merger events, the intra-cluster medium (ICM) is heated by shocks and is believed to become turbulent. Part of the energy involved in these processes is converted into non-thermal phenomena that exhibit themselves in the radio band as halo and relic emissions (e.g. Brunetti & Jones 2014, for a review). Both radio sources are diffuse cluster-scale sources with steep spectra[1] ($\alpha \gtrsim 1$). Radio haloes are generally morphologically connected with the X-ray emission of the hosting cluster, whereas radio relics are elongated, polarized and found in cluster peripheries (e.g. Feretti et al. 2012, for an observational overview). In particular, radio relics are believed to form at the gigantic shocks that are generated in major mergers, where cosmic ray electrons (CRe) are (re)accelerated (see Brüggen et al. 2012; Brunetti & Jones 2014, for reviews). This scenario is supported by the arc-shaped morphologies of relics, their high level of polarization and by the fact that an increasing number of shocks have been detected at the location of radio relics (e.g. Akamatsu & Kawahara 2013; Bourdin et al. 2013; Shimwell et al. 2015; Botteon et al. 2016; Eckert et al. 2016). The main difficulty in the understanding of the origin of radio relics resides in the low Mach number ($\mathcal{M} \lesssim 3$–4) associated with merger shocks. The acceleration efficiency at these weak shocks is indeed expected to be small and in several cases it is in tension with the observational requirements (e.g. Markevitch et al. 2005; Macario et al. 2011; Kang, Ryu & Jones 2012; Pinzke, Oh & Pfrommer 2013; Kang et al. 2014; Botteon et al. 2016; van Weeren et al. 2016).

ACT-CL J0102–4915 is the most massive cluster detected in the far Universe, at a redshift of $z = 0.87$ (Menanteau et al. 2012). For its extraordinary mass of $M_{500} \sim 8.8 \times 10^{14}\ \mathrm{M}_{\odot}$ (Planck Collaboration XXIX 2014), it is also known with the nickname of 'El Gordo'. The cluster was first discovered by its strong Sunyaev–Zel'dovich (SZ) signal (Marriage et al. 2011) and later confirmed through optical and X-ray observations. The system is in a complex merger state, as revealed by the double peaked galaxy distribution and the elongated morphology of its hot ($kT \sim 15$ keV) ICM (Menanteau et al. 2010, 2012). In the radio band, a tenuous halo and a double relic system at the cluster NW and SE X-ray boundaries were discovered (Lindner et al. 2014).

In this paper we report the discovery of a strong shock associated with a radio relic in 'El Gordo' cluster. In particular, our joint *Chandra* and *Giant Metrewave Radio Telescope* (GMRT) analysis provides interesting insights about the origin of the relic. Throughout the paper, we assume a concordance ΛCDM cosmology with $H_0 = 70\ \mathrm{km\ s^{-1}\ Mpc^{-1}}$, $\Omega_\mathrm{m} = 0.3$ and $\Omega_\Lambda = 0.7$, in which 1 arcsec $= 7.713$ kpc at the cluster redshift ($z = 0.87$). Reported uncertainties are 68 per cent, unless stated otherwise.

2 OBSERVATIONS AND DATA REDUCTION

2.1 X-ray data reduction

'El Gordo' was observed three times (ObsID: 12258, 14022, 14023) with *Chandra* in ACIS-I configuration and VFAINT mode for a

★ E-mail: botteon@ira.inaf.it

[1] $S_\nu \propto \nu^{-\alpha}$, with α spectral index.

total exposure time of 360 ks. We carried out the standard data reduction by using CIAO 4.7 and *Chandra* CALDB 4.6.9. In particular, soft proton flares were inspected analysing the light curves extracted from the S3 chip in the 0.5–2 keV band for each ObsID and removed using the `lc_clean` routine. We then used the `merge_obs` task to make the final 0.5–2 keV cleaned image (340 ks) shown in Fig. 1(a).

We created a single exposure-corrected point spread function (PSF) map with minimum size for the merged image by combining the PSF and exposure maps of each ObsID. Once the PSF of the instrument is known, the `wavdetect` task allows us to identify discrete sources in the surface brightness (SB) image of the cluster. These were detected using wavelet radii of 1, 2, 4, and 8 pixels, confirmed by eye and excluded in the SB profile analysis. In order to create a single background image, the `reproject_event` task was used to match the background templates to the corresponding event files for every ObsID. This single background image was normalized by counts in the band 9.5–12 keV and subtracted during the SB analysis.

Dealing with spectral analysis of low SB sources as in the case of cluster outskirts requires a detailed treatment of the astrophysical and instrumental background emission. In this respect, we modelled the sky component due to the Galactic emission with two thermal plasmas with $kT_1 = 0.14$ keV and $kT_2 = 0.25$ keV, the cosmic X-ray background with an absorbed power law with photon index $\Gamma = 1.4$ and the ACIS-I particle background by using the analytical approach proposed by Bartalucci et al. (2014). Spectra were extracted in the same region for every ObsID and simultaneously fitted in the 0.5–11 keV energy band with the package XSPEC v12.9.0o. Since the low X-ray count rate, we kept the metal abundance of the `APEC` model, which accounts for the ICM thermal emission, fixed at the value of 0.3 $Z_\odot$ (solar abundance table by Anders & Grevesse 1989) and used Cash statistics during the fits.

2.2 Radio data reduction

Archival GMRT 610 MHz observations of 'El Gordo' (project code 22_001, PI: R. R. Lindner) taken on 2012 August 26 were analysed using the Astronomical Image Processing System (AIPS). The GMRT Software Backend was used to record the parallel polarization products RR and LL with a bandwidth of 33.3 MHz divided into 256 channels. The source 3C48 was used for flux and bandpass calibration and the calibrator 0024 − 420 was used for phase calibration towards the target. The total on-target observing time was 170 min. Standard steps of flagging (excision of bad data) and calibration were carried out. The resulting calibrated visibilities towards the target were split and used for imaging. A few rounds of phase-only self-calibration and a round of amplitude and phase self-calibration were carried out to improve the sensitivity of the image. The final image with visibilities weighted according to `ROBUST 0` in the task `IMAGR` and resolution 11 arcsec × 4.8 arcsec (position angle 4.°8) is presented in Fig. 1(b). The image was corrected for the GMRT primary beam using the task `PBCOR`. The off-source noise level is 50 μJy b^{-1} and a 10 per cent error on the absolute flux calibration scale was assumed.

As a preliminary result of new GMRT data, we also used observations taken at 327 MHz (project code 25_023, PI: R. Kale) to perform spectral analysis. The complete analysis of the new radio data set will be presented in the forthcoming paper (Kale et al., in preparation).

3 RESULTS

3.1 X-ray/radio analysis

'El Gordo' X-ray emission remarkably recalls the famous 'Bullet' cluster (Markevitch et al. 2002): a dense cool core ($kT \sim 6$ keV) is moving in the SE–NW direction producing a prominent cold front (Menanteau et al. 2012) which is expected to follow a shock wave (e.g. Vikhlinin, Markevitch & Murray 2001; Markevitch et al. 2002). The cluster is elongated along the merger direction and presents a couple of X-ray tails that give to the system a comet-like morphology (Fig. 1a).

Our 610 MHz radio image of 'El Gordo' recovers extended emission better than previously done by Lindner et al. (2014, figs 2 and 15) as we considered baselines down to 0.2 kλ (instead of 0.48 kλ). This allows us to study the morphology of the diffuse sources in more detail. In our image shown in Fig. 1(b), the prominent and elongated radio halo connects a pair of radio relics, located in opposite directions at the NW and SE edges of the cluster X-ray emission (Fig. 1c). The strongest part of the halo coincides with the disrupted cluster core, whereas a radio tail appears to remarkably follow the northern tail visible in the X-rays (Fig. 1c).

Our work is focused on the NW radio relic, whose flux densities at 610 and 327 MHz are $F_{610} = 27.5 \pm 2.8$ mJy and $F_{327} = 64.6 \pm 6.6$ mJy, respectively. These result in a radio spectral index $\alpha = 1.37 \pm 0.20$. The flux density of the relic at 2.1 GHz measured by Lindner et al. (2014) with the *Australia Telescope Compact Array* implies $\alpha \sim 1.5$ from 2100 to 327 MHz, which is consistent with what we estimated in the narrower frequency range. Nevertheless, we will use the spectral index from 610 to 327 MHz since it is taken from two high sensitivity images obtained from GMRT observations with matched inner-*uv* coverage ($uv_{\rm min} = 0.2$ kλ).

3.2 Relics and shocks

Double relics have been observed in different systems (e.g. de Gasperin et al. 2014) and are believed to form in mergers between two clusters with similar mass where diametrically opposite shocks move outwards along the merger axis (re)accelerating particles (van Weeren et al. 2011a). Menanteau et al. (2012) pointed out the possible presence of a couple of shocks by analysing a 60 ks *Chandra* unsharp-masked image of 'El Gordo'. For these reasons we created the unsharp-masked images shown in Fig. 2 and searched for sharp edges in the X-ray SB image, identifying at least one discontinuity in the cluster. We used PROFFIT v1.3.1 (Eckert, Molendi & Paltani 2011) to extract the SB profiles in the red sectors shown in Fig. 3, where the NW relic stands out. An underlying broken power-law density profile is usually adopted to describe the SB in the presence of a discontinuity. In the case of spherical symmetry, the downstream density $\rho_{\rm d}$ is higher by a factor of $\mathcal{C} \equiv \rho_{\rm d}/\rho_{\rm u}$, with $\rho_{\rm u}$ upstream density, at the shock putative distance $r_{\rm sh}$. In formula

$$\rho_{\rm d}(r) = \mathcal{C}\rho_0 \left(\frac{r}{r_{\rm sh}}\right)^{a_1}, \quad \text{if} \quad r \leq r_{\rm sh}$$
$$\rho_{\rm u}(r) = \rho_0 \left(\frac{r}{r_{\rm sh}}\right)^{a_2}, \quad \text{if} \quad r > r_{\rm sh} \qquad (1)$$

where ρ_0 is the density normalization, a_1 and a_2 are the power-law indices and r is the radius from the centre of the sector (in Fig. 3; RA: +15.°7275, DEC: −49.°2724, J2000). We used this density shape to fit the X-ray SB keeping all parameters of the model free to vary.

We first report results concerning sector 1+2 [opening angle (OA): 30° − 98°] because it covers the whole extension of the

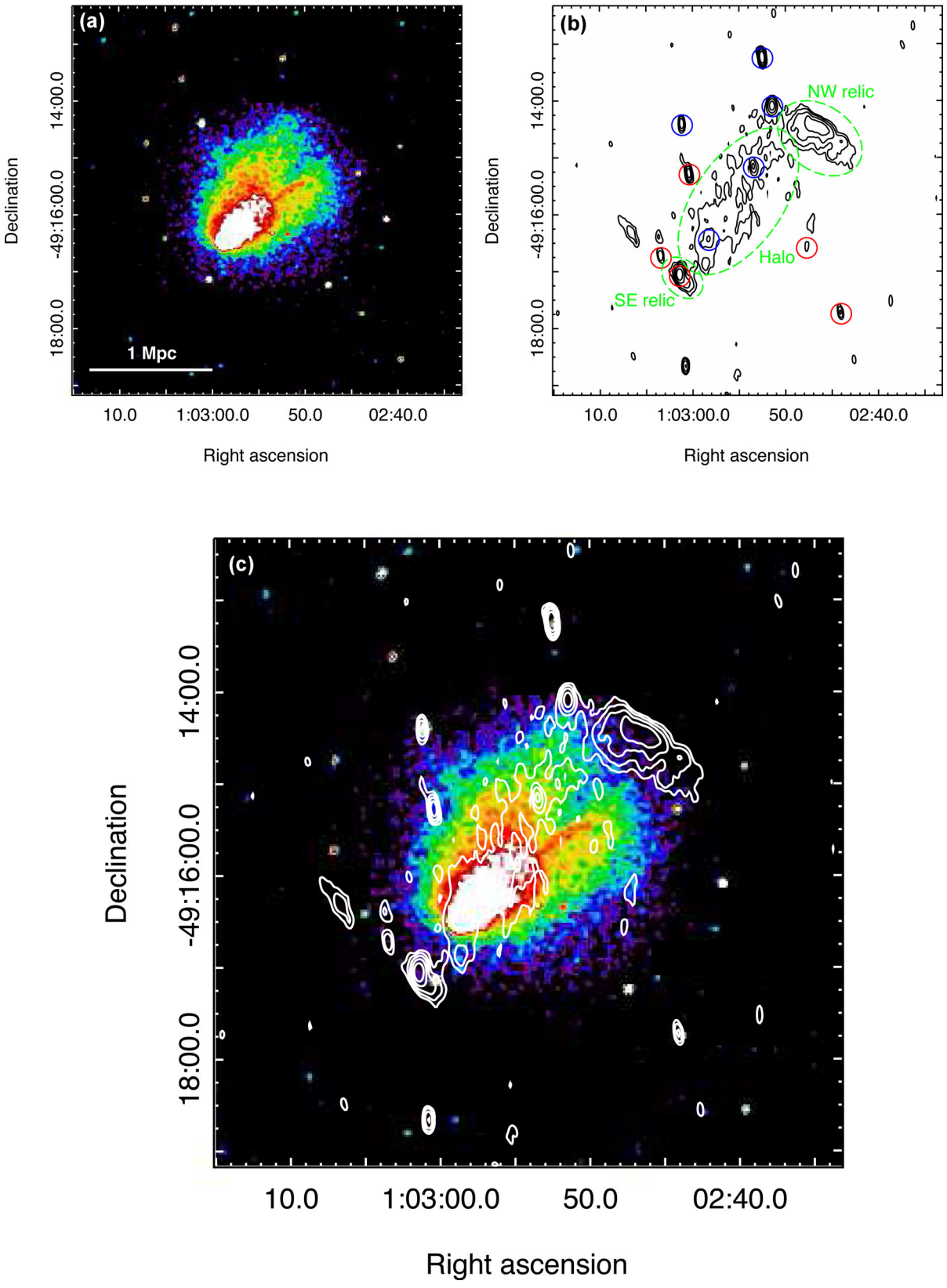

Figure 1. 'El Gordo' galaxy cluster. (a) *Chandra* 0.5–2 keV band exposure-corrected image smoothed on a 3 arcsec scale. (b) GMRT 610 MHz radio emission at a resolution of 11 arcsec × 4.8 arcsec. The 1σ noise level is 50 μJy b^{-1}; contours are drawn at levels of $3\sigma \times (-1, 1, 2, 4, 8, 16)$. Circles denote the compact radio sources identified in Lindner et al. (2014) as cluster members (red) or not (blue). (c) In the *Chandra*/GMRT comparison the location of the radio relics at the cluster X-ray boundaries and the spatial connection between the halo and the northern X-ray tail are evident.

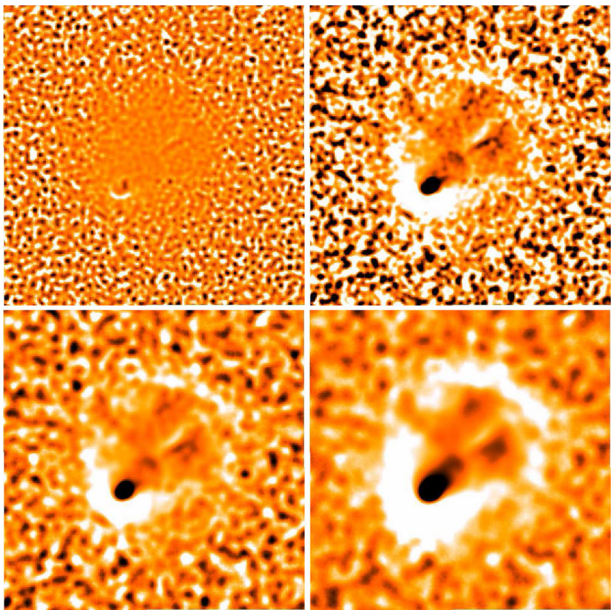

Figure 2. Unsharp-masked *Chandra* images for 'El Gordo' cluster created by subtracting images convolved with Gaussians with σ_1 and σ_2 and dividing by the sum of the two. From top left panel in clockwise order (σ_1, σ_2) = (3 arcsec, 5 arcsec), (3 arcsec, 20 arcsec), (7 arcsec, 30 arcsec), (5 arcsec, 20 arcsec).

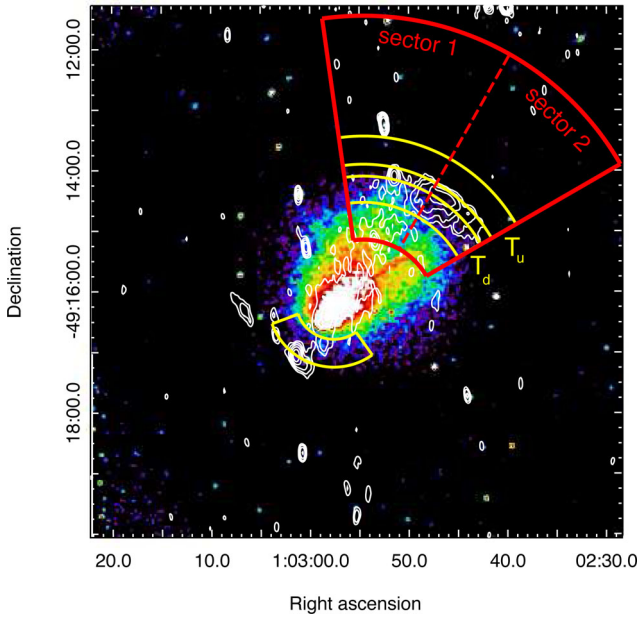

Figure 3. Radio/X-ray overlay of 'El Gordo'. Red sectors delineate the SB extracting regions. Spectral analysis was performed in the yellow sectors. Colours and contours are the same reported in Fig. 1.

feature shown in Fig. 2 and it gives the maximum SB drop with the best statistics (a discussion on the sector choice is presented in Section 3.2.1). In Fig. 4, we report the best broken power-law model fit, which is in excellent agreement with data. We detect a large SB drop, corresponding to a density compression factor

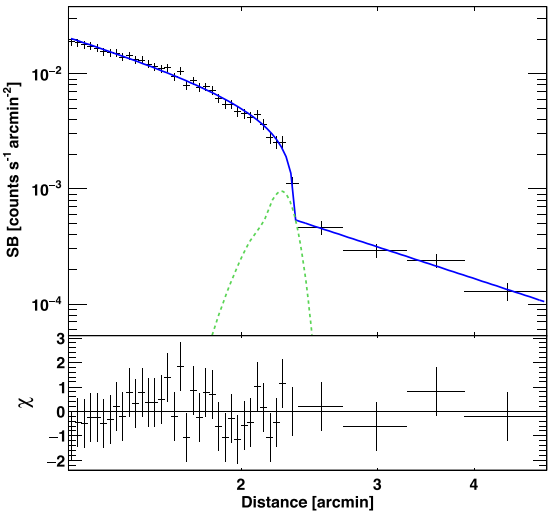

Figure 4. X-ray SB profile in the 0.5–2 keV band extracted in sector 1+2 (Fig. 3). The data were rebinned to reach a minimum signal-to-noise ratio of 7. The green dashed line shows the NW radio relic brightness profile (in arbitrary units).

$\mathcal{C} = 3.4^{+0.4}_{-0.3}$, co-spatially located with the relic. For a shock, the Rankine–Hugoniot (RH) jump conditions for a monatomic gas

$$\mathcal{C} \equiv \frac{\rho_d}{\rho_u} = \frac{4\mathcal{M}^2_{SB}}{\mathcal{M}^2_{SB} + 3} \tag{2}$$

would lead to a Mach number $\mathcal{M}_{SB} = 4.1^{+3.4}_{-0.9}$. A $\mathcal{M} > 3$ shock is quite a rarity in galaxy clusters and so far only two of them have been detected ($\mathcal{M} = 3.0 \pm 0.4$ in the 'Bullet' cluster, Markevitch 2006; $\mathcal{M} = 3.0 \pm 0.6$ in A665, Dasadia et al. 2016).

Shocks heat the downstream gas and this allows us to distinguish them from cold fronts, other kinds of SB discontinuities found in galaxy clusters with inverted temperature jumps (e.g. Markevitch & Vikhlinin 2007). For this reason we performed spectral analysis in the yellow sectors shown in Fig. 3. Spectra for sector 1+2 are reported in Fig. 5. We found evidence of a very high downstream temperature, $kT_d = 17.9^{+3.3}_{-2.8}$ keV, while only a lower limit to the upstream one was obtained, $kT_u > 6.1$ keV. In principle, this is not enough to confirm the shock nature of the discontinuity but, similarly to the E shock in the 'Bullet' cluster (Shimwell et al. 2015), the presence of a cold front is very unlikely because it would imply a too high temperature ($kT_u > 20$ keV) at such a large cluster distance.

Although current data do not allow us to measure a temperature jump at the position of the shock, we can use the lower limit to such a jump to provide independent constraints on the shock Mach number. According to RH conditions, the upstream and downstream temperature are related by

$$\frac{T_d}{T_u} = \frac{5\mathcal{M}^4_{kT} + 14\mathcal{M}^2_{kT} - 3}{16\mathcal{M}^2_{kT}} \tag{3}$$

which implies $\mathcal{M}_{kT} < 2.9$ if we insert the upper 1σ limit of T_d and the lower limit on T_u. We anticipate that this value is consistent with the Mach number inferred from SB jump once systematic errors are taken into account (see the following section).

A visual inspection of Fig. 1(a) suggests the presence of a drop in SB also at the position of the SE relic. A shock in this region is expected due to the presence of the radio relic and in analogy

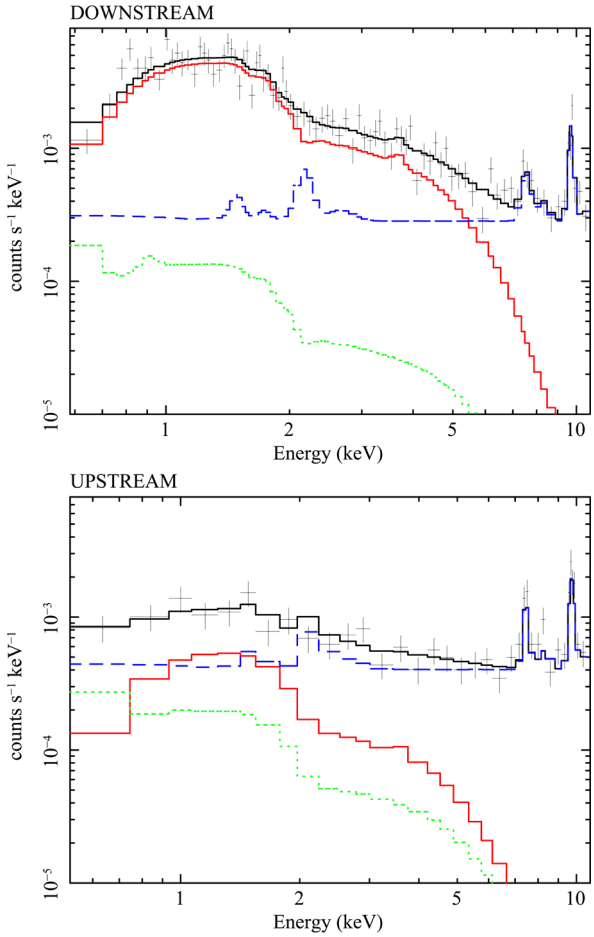

Figure 5. Downstream (top) and upstream (bottom) spectra of sector 1+2. Data points are shown in black together with the best-fitting model. Different colours highlight the model components: the cluster emission (in solid red), the particle background (in dashed blue) and the sky background (in dotted green). The c-stat/d.o.f. of the fits are 203/168 and 128/115 for the downstream and upstream spectrum, respectively. Although spectra were simultaneously fitted, only one ObsID was reported in order to avoid confusion in the plot.

with the 'Bullet' cluster (Markevitch et al. 2002). However, current data do not allow us to characterize statistically the SB drop because of the low X-ray counts in this region. Nevertheless, we found evidence for high temperature in the putative downstream gas, $kT_{\rm d} = 30.1^{+10.5}_{-6.2}$ keV in the yellow sector in the SE (Fig. 3), somewhat supporting this possibility. Since typical temperatures in cluster outskirts are of a few keV, such a high $kT_{\rm d}$ would likely imply a $\mathcal{M} \gtrsim$3.5–4 shock.

3.2.1 Systematic errors on X-ray analysis

Results in the previous section are based on measurements obtained for a particular sector (1+2). This entirely covers the feature found in the unsharp-mask images (Fig. 2) and allows the best characterization of the SB jump due to the statistics of the fit.

We checked the impact due to the choice of the SB extracting region in the determination of the NW X-ray discontinuity and the resulting Mach number. First, we re-performed SB and spectral analysis by splitting the red and yellow sectors of Fig. 3 in two sub-regions; the dashed line distinguishes between sector 1 (OA: 60°.5–98°), which is oriented in the N direction, and sector 2 (OA: 30°−60°.5), which is in the NW direction and better overlaps the relic. In both regions, the SB profile is well described by a compression factor $\mathcal{C} \gtrsim 3$, implying $\mathcal{M}_{\rm SB} \gtrsim 3$.

We then repeated the SB analysis by excluding data at $r < 2$ arcmin and keeping the discontinuity distance frozen at the values found in the 1.2–4.9 arcmin radial range. Although with a large error, spectral analysis allowed us to constrain the upstream temperature in sector 1, implying a 68 per cent confidence interval estimate for the Mach number $\mathcal{M}_{\rm kT} = 1.9 - 3.4$ (taking into account the asymmetric errors on the two temperatures), whereas only lower limits to $kT_{\rm u}$ can be obtained in sectors 1+2 and 2. The results of the fits obtained for the three regions are summarized in Table 1.

Finally, we checked the variation on $\mathcal{M}_{\rm SB}$ in sector 1+2 due to different shock curvature radii from the best-fitting value found in Fig. 4 ($r_{\rm curv} \sim 1$ Mpc). Results are reported in Table 2 and the impact of $r_{\rm curv}$ on the shock compression factor is presented in Fig. 6.

Spectral analysis requires a careful determination of the background sources and its systematic uncertainties. In this respect, we varied background normalization levels within $\pm 1\sigma$ and re-performed spectral fits. We achieved results consistent with the reported cluster parameters within 1σ. Nonetheless, we highlight that the measurement of high temperatures is critical with *Chandra* given its low effective area at energies higher than 5 keV, in particular the estimated confidence range may not reflect entirely the true statistical and systematic error range.

As a final test, a more complex model of a two-temperature thermal plasma was adopted to fit the downstream spectra. In this case, the high-T component is not constrained while the low-T component gives unreasonably low temperatures (e.g. $kT_{\rm high} = 21.2$ keV and $kT_{\rm low} = 2.2^{+4.0}_{-1.2}$ keV, for sector 1+2). As pointed out in the case of the Coma cluster (Gastaldello et al. 2015), the low-T component mitigates the fit residuals at low energy rather than describing a physical condition. The high-T spectral component instead supports the presence of a high temperature plasma in the downstream region.

3.3 Constraints on the downstream magnetic field

Relativistic electrons scattering with the cosmic microwave background (CMB) photons is expected to produce inverse Compton (IC) emission. From the ratio between radio and X-ray emission it is possible to constraint the magnetic field in the source region (e.g. Blumenthal & Gould 1970). For this reason we preformed spectral analysis in a region enclosing the NW relic and introduced, in addition to the canonical thermal model for the ICM, a power law in the spectral fit.

We assume that the IC spectrum is a power law with photon index related to the synchrotron spectral index via $\Gamma = \alpha + 1$. Initially, we set $\Gamma = 2.37$ (see Section 3.1) and kept it frozen in the fit while thermal parameters were free to vary. In this case we obtain 0.5–2 keV upper limit to the non-thermal component $F_{[0.5-2\,{\rm keV}]} < 6.76 \times 10^{-15}$ erg s^{-1} cm^{-2}.

The IC measurement is a very complicated issue and can be influenced by several factors. We investigated the impact on IC flux estimation by: using the IC power-law slope in the range 2.17–2.57 (consistently with the values reported in Section 3.1), keeping the temperature frozen at 13.5 and 17 keV (which covers a range of kT obtained for different sector choices in the relic region), varying background normalization levels within $\pm 1\sigma$ and re-performing the fits in the 0.7–11 and 0.9–11 keV energy bands. In summary, we

Table 1. Results of the SB and spectral fits of the regions shown in Fig. 3. Fits in the 2.0–4.9 arcmin radial range were made keeping r_{sh} frozen at the best-fitting value achieved in the wider range.

Sector	Radial range (arcmin)	r_{sh} (arcmin)	$\mathcal{C}$	$\mathcal{M}_{SB}$	χ^2/d.o.f.	kT_d (keV)	kT_u (keV)	$\mathcal{M}_{kT}$
1	1.2−4.9	$2.359^{+0.006}_{-0.004}$	$3.5^{+0.7}_{-0.5}$	> 3.0	20.4/32	$18.3^{+4.1}_{-3.2}$	$6.8^{+10.8}_{-2.8}$	1.9−3.4
	2.0−4.9		$3.1^{+0.7}_{-0.5}$	$3.2^{+4.3}_{-0.8}$	0.9/6			
2	1.2−4.9	$2.321^{+0.065}_{-0.041}$	$3.7^{+1.2}_{-0.7}$	> 3.0	35.4/24	$15.8^{+7.9}_{-3.9}$	>6.1	<3.1
	2.0−4.9		$4.2^{+1.6}_{-0.9}$	> 3.8	7.3/2			
1+2	1.2−4.9	$2.338^{+0.007}_{-0.005}$	$3.4^{+0.4}_{-0.3}$	$4.1^{+3.4}_{-0.9}$	18.9/34	$17.9^{+3.3}_{-2.8}$	>6.1	<2.9
	2.0−4.9		$3.4^{+0.5}_{-0.4}$	$4.1^{+6.7}_{-1.1}$	5.0/8			

Table 2. Impact on the SB profile fits in sector 1+2 due to different shock curvature radii. Note that $r_{curv} \sim 1$ Mpc in Fig. 4.

r_{curv} (Mpc)	$\mathcal{C}$	$\mathcal{M}_{SB}$	χ^2/d.o.f.
0.6	2.5 ± 0.2	$2.2^{+0.3}_{-0.2}$	96.1/48
0.8	3.1 ± 0.3	$3.2^{+0.9}_{-0.6}$	91.5/52
1.2	$3.4^{+0.4}_{-0.3}$	$4.1^{+3.4}_{-0.9}$	41.0/45
1.4	$3.2^{+0.4}_{-0.3}$	$3.5^{+1.7}_{-0.6}$	24.7/28
1.6	3.1 ± 0.3	$3.2^{+0.9}_{-0.6}$	37.5/27
1.8	$2.9^{+0.3}_{-0.2}$	$2.8^{+0.6}_{-0.3}$	43.1/25

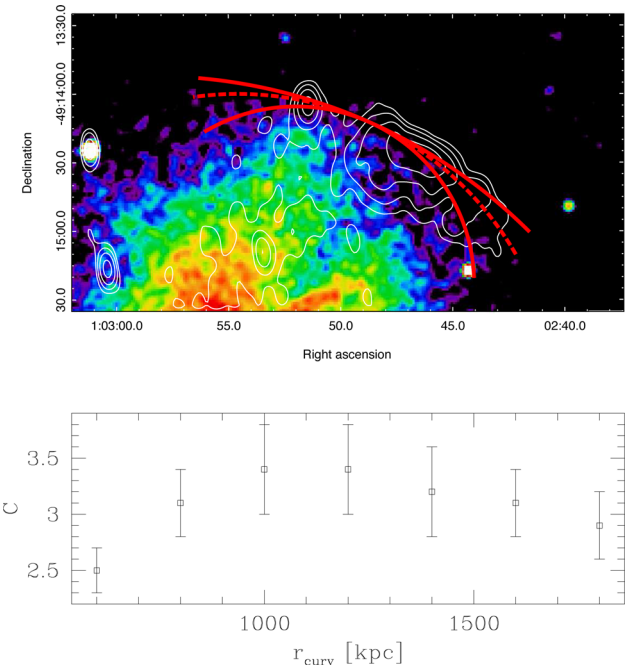

Figure 6. In the top panel we show the difference between the best-fitting curvature radius of ∼1 Mpc (dashed line) and the two extreme cases with $r_{curv} = 600$ and 1800 kpc (lower and upper solid lines, respectively). In the bottom panel we compare compression factors achieved for different values of r_{curv} (see Table 2).

found upper limits in the range $(2.95-8.51) \times 10^{-15}$ erg s^{-1} cm^{-2} for the IC flux, representing $\lesssim 50$ per cent of the thermal model flux in the same energy band (0.5–2 keV). However, in the case of temperature frozen at 17 keV, the fits formally result in a IC detection both for $\Gamma = 2.17$ and 2.57; we do not consider these detections solid enough due to the systematics related to the presence of multi-temperature components and background characterization. We further explore the possibility of IC detection in Section 4.2.

By using our upper limits to IC flux, we conservatively obtained[2] the following lower limits to the downstream magnetic field strength: $B \geq 3.1$ μG for $\Gamma = 2.17$, $B \geq 4.9$ μG for $\Gamma = 2.37$ and $B \geq 7.6$ μG for $\Gamma = 2.57$. These values are in line with other estimates for radio relics (e.g. Bonafede et al. 2009; Finoguenov et al. 2010; van Weeren et al. 2010, 2011b).

3.4 Acceleration efficiency

The relic–shock connection is nowadays supported by many observational studies. Nevertheless, theoretical models of relic formation are challenged by the low Mach numbers associated with cluster shocks. In fact, the commonly adopted diffusive shock acceleration (DSA) model is severely challenged for weak shocks if CRe are accelerated by the thermal pool (e.g. Brunetti & Jones 2014, for review). A connected problem is the ratio of cosmic ray protons and electrons that would be generated at these shocks and that current γ-ray *Fermi* limits constrain at values that are significantly smaller than that in supernova remnants (e.g. Vazza et al. 2015, 2016).

If the downstream synchrotron luminosity emitted at frequency $\geq\nu_0$ originates from electrons in steady-state conditions, the bolometric ($\geq\nu_0$) synchrotron luminosity that is generated via shock acceleration from a shock with speed V_{sh} and surface S can be estimated as

$$\int_{\nu_0} L(\nu)\,\mathrm{d}\nu \simeq \frac{1}{2}\eta_e \Psi \rho_u V_{sh}^3 \left(1 - \frac{1}{\mathcal{C}^2}\right) \frac{B^2}{B_{cmb}^2 + B^2} S \qquad (4)$$

where η_e is the efficiency of electron acceleration,

$$\Psi = \frac{\int_{p_{min}} N_{inj}(p) E\, dp}{\int_{p_0} N_{inj}(p) E\, dp} \qquad (5)$$

accounts for the ratio of the energy flux injected in 'all' electrons and those visible in the radio band ($\nu \geq \nu_0$), p_0 is the momentum of the relativistic electrons emitting the synchrotron frequency ν_0 in a magnetic field B and $B_{cmb} = 3.25(1+z)^2$ μG accounts for IC scattering of CMB photons. The injection spectrum of accelerated CRe is given by

$$N_{inj}(p) = (\delta_{inj} + 2) p^{-\delta_{inj}} \int_{p_{min}}^{p} x^{\delta_{inj}-1} N_u(x)\,\mathrm{d}x, \qquad (6)$$

where N_u is the spectrum of seed particles upstream. In the case of CRe acceleration from the thermal pool this is $N_u \propto p^{-\delta_{inj}}$, where

[2] Calculations were obtained using equation (32) in Brunetti & Jones (2014).

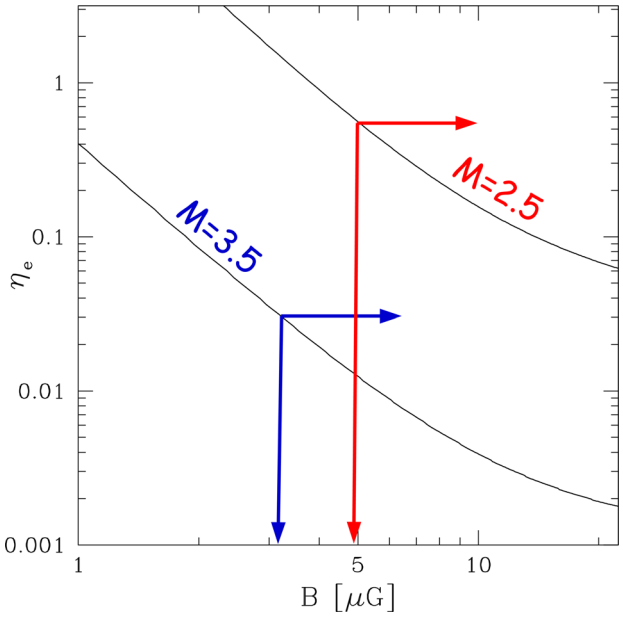

Figure 7. Electron acceleration efficiency versus magnetic field downstream in the NW shock in 'El Gordo'. Black lines represent efficiencies evaluated for a Mach number with $\mathcal{M} = 2.5$ (top) and 3.5 (bottom). Calculations were obtained with $p_{\rm min} = 0.1 m_{\rm e} c$ in equation (6). Vertical lines denote the lower limits on the downstream magnetic field strength achieved from the lack of IC emission from the relic.

$\delta_{\rm inj} = 2(\mathcal{M}^2 + 1)/(\mathcal{M}^2 - 1)$, implying a synchrotron spectral index $\alpha = \delta_{\rm inj}/2$ in the case of steady-state conditions (e.g. Blandford & Eichler 1987).

In Fig. 7 we report the acceleration efficiency that is necessary to explain the radio luminosity observed in the NW relic assuming DSA of thermal electrons upstream.

We assumed shock Mach numbers $\mathcal{M} = 3.5$ and 2.5, in line with the values derived from the X-ray analysis. These Mach numbers would imply a synchrotron spectrum of the relic $\alpha = 1.18$ and 1.38, respectively, that are in line with radio measurements (Section 3.1). Calculations were obtained assuming upstream number density and temperature 2.4×10^{-4} cm^{-3} and 6.1 keV, respectively, and a surface of the relic $S = \pi \times 350^2$ kpc^2.

In Fig. 7 we also show the lower limits to the magnetic field in the relic that are derived from the upper limits to the IC flux assuming the two values of the spectral index (Section 3.3).

Despite the fact that we are dealing with a high-velocity shock, $V_{\rm sh} \sim 4000$ km s^{-1}, we note that the efficiency of CRe acceleration that is requested to explain the total radio relic luminosity is large. This is due to the fact that the NW relic in the 'El Gordo' is one of the most luminous radio relics known so far and because, for few μG magnetic fields, most of the CRe energy is radiated via IC emission (due to the high redshift of the cluster). Still, contrary to the case of weaker shocks (see e.g. A754, Macario et al. 2011; 1RXS J0603.3+4214, van Weeren et al. 2016; A115, Botteon et al. 2016), we conclude that in this case DSA of thermal electrons is still a viable option. Indeed, for Mach number $\gtrsim$3.5 the electron acceleration efficiency appears energetically viable $\eta_{\rm e} \leq 0.01$, whereas for $\mathcal{M} \sim$ 3–3.5 additional mechanisms of pre-acceleration of thermal electrons downstream (see Guo, Sironi & Narayan 2014a,b) may be required.

The other possibility is that the NW relic is due to shock re-acceleration of seed (relativistic or supra-thermal) electrons. In this case the efficiency necessary to explain the radio emission is much smaller simply because the bulk of the energy is channelled directly into highly relativistic particles (equation 6, e.g. Markevitch et al. 2005; Kang et al. 2012). Seeds can be broadly distributed in the cluster outskirts where the lifetime of 100 MeV electrons is very long (e.g. Pinzke et al. 2013; Donnert et al. 2016) or they can be in radio ghost/clouds generated by past AGN activity (e.g. Kang & Ryu 2016). The two possibilities have different predictions on the upstream synchrotron emission that in principle can be tested with very deep radio observations, but that are well beyond the aim of our paper.

4 DISCUSSION

4.1 Overall considerations

'El Gordo' is a high-redshift ($z = 0.87$; Menanteau et al. 2012) and high-mass ($M_{500} \sim 8.8 \times 10^{14}$ M$_\odot$; Planck Collaboration XXIX 2014) galaxy cluster. It is the most distant massive cluster with the brightest X-ray and SZ emission and the farthest hosting diffuse radio sources (halo and relics). Our study makes it is also the most distant cluster where a shock (with one of the highest Mach number) has been detected.

Optical and X-ray observations revealed that 'El Gordo' is in a merging state (Menanteau et al. 2010, 2012). Recent numerical simulations were able to reproduce the overall system properties assuming a nearly head on major merger (Donnert 2014; Molnar & Broadhurst 2015; Ng et al. 2015; Zhang, Yu & Lu 2015).

Double relic systems are expected to trace shocks moving outwards in cluster outskirts. So far, studies on 'El Gordo' were mainly focused on the SE relic located in front of the dense cool core, which is expected to follow a shock in analogy with the well-know 'Bullet' cluster case (Markevitch et al. 2002). However, current X-ray data do not allow us to characterize the jump in this region because of the low statistics. We instead discovered a $\mathcal{M} \gtrsim 3$ shock spatially coincident with the NW relic. Our detection is based on the *Chandra* SB jump. Although with large uncertainties, spectral analysis is also consistent with the presence of a strong shock in the ICM. Further indications of the shock are given by the unsharp-masked images of Fig. 2. We also mention the striking similarity between 'El Gordo' shock/reverse-shock and X-ray morphology with A2146 (Russell et al. 2010, 2012) even though the latter is a less massive system ($M_{500} \sim 3.8 \times 10^{14}$ M$_\odot$, Planck Collaboration XXIX 2014) and does not host any radio relics at the sensitivity level of current observations (Russell et al. 2011).

4.2 Hints of inverse Compton emission

The search for IC emission from galaxy clusters has been undertaken for many years with many instruments. However, no confirmed detection has been obtained so far. The most famous dispute in this field is regarding the case of the nearby Coma cluster (Fusco-Femiano et al. 1999, 2004; Rephaeli, Gruber & Blanco 1999; Rephaeli & Gruber 2002; Rossetti & Molendi 2004; Fusco-Femiano, Landi & Orlandini 2007; Wik et al. 2009, 2011; Gastaldello et al. 2015). The excellent spatial resolution and good spectral capabilities of the *Chandra* satellite allow to minimize the contamination from the thermal X-ray emission and open the possibility to search for non-thermal emission also in the soft X-ray band (e.g. Million & Allen 2009).

'El Gordo' is a perfect target to search for IC emission. It hosts a bright radio relic in an external region with low thermal SB and it

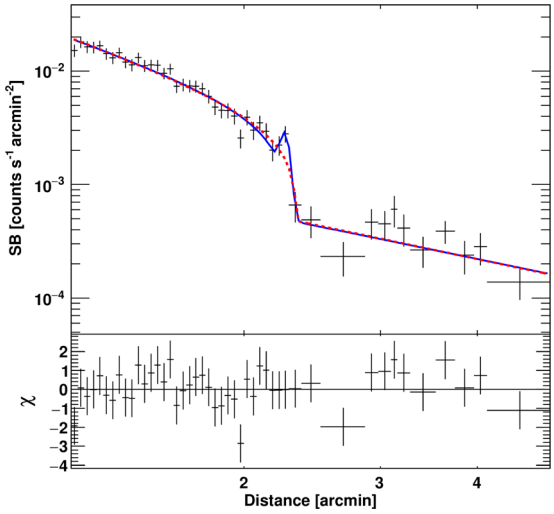

Figure 8. X-ray SB profile in the 0.5–2 keV band extracted in a region enclosing the NW relic. The broken power-law fit is reported in dashed red. The SB excess just before the discontinuity, i.e. at the relic location, for which we speculate a IC origin was modelled by adding a Gaussian component to the broken power-law model (solid blue line). Residuals of the latter model are displayed in the bottom panel. The data were rebinned to reach a minimum signal-to-noise ratio of 3.

is at high redshift ($z = 0.87$), where the equivalent CMB magnetic field strength is large, $B_{\rm cmb} = 3.25(1+z)^2 = 11.4$ μG.

We used the deep *Chandra* observations to look for IC signatures in the NW relic (Section 3.3). In the case the temperature is frozen at 17 keV, the spectral analysis provides a formal detection and a significant fraction (up to 40–50 per cent) of the X-ray brightness across the relic would be contributed by IC emission from the relic itself. This should be visible in the X-ray images and profiles across the relic. For this reason we extracted a SB profile in the 0.5–2.0 keV across a narrow sector (OA: 37.°2–67.°5) containing the NW radio relic. The fit of a broken power-law model (equation 1) in this restricted region provides a good description of the SB jump, as shown in Fig. 8 (dashed red line), leading to χ^2/d.o.f. = 48.5/41. However, a SB excess is present at the location of the relic. For this reason we also attempt to fit the SB by adding a Gaussian component to the downstream power law. The addition of this Gaussian improves the fit (Fig. 8, solid blue line) with χ^2/d.o.f. = 40.3/38. Slightly different sector centres and apertures do not influence this excess. The Gaussian component coincident with the relic could represent an excess due to IC emission from electrons in the relic. The excess flux associated with the Gaussian component is in line with that expected from the spectral analysis. The combination of this excess with the formal detection of IC emission obtained from the spectral analysis (with kT frozen) is tantalizing; however deeper observations (i.e. >500 ks) are required to firmly conclude about this possible detection.

5 CONCLUSIONS

We presented an X-ray/radio study of the famous 'El Gordo' cluster located at $z = 0.87$ focusing on the non-thermal activity in the cluster.

Our GMRT radio observations at 610 and 327 MHz confirmed the presence of a halo and a system of double relics. These represent the most distant diffuse radio sources detected in a galaxy cluster so far. The halo is quite elongated in the NW–SE, i.e. in the merger direction, and remarkably follows the ICM emission of the northern X-ray tail. The two relics are found at the boundaries of the X-ray emission. We focused on the NW relic which has a synchrotron spectral index $\alpha = 1.37 \pm 0.20$ between 610 and 327 MHz.

The deep *Chandra* observations (340 ks) allowed us to discover a shock at the position of the NW relic. The SB profile taken in the NW outskirts of the cluster abruptly drops at the relic location. The density compression factor $\mathcal{C} \gtrsim 3$ and the high downstream temperature provide the indication of a strong shock ($\mathcal{M} \gtrsim 3$) in the ICM. This is one of the three strongest shocks detected in galaxy clusters and the most distant ($z = 0.87$) observed so far.

The detection of a shock co-spatially located with a relic strongly supports the relic–shock connection. The NW shock in 'El Gordo' cluster allows us to study particle acceleration in a rare regime of strong shock. We found that DSA of thermal electrons is consistent with measured synchrotron spectrum. Nonetheless, only shocks with $\mathcal{M} > 3.5$ appear energetically viable while for weaker shocks re-acceleration models would be preferred.

The presence of relativistic particles emitting a bright synchrotron relic at $z = 0.87$ makes 'El Gordo' a suitable cluster candidate to search for IC emission from the relic. From the X-ray spectral analysis we obtained possible hints for IC emission from the relic; however we could not firmly conclude the presence of IC excess and conservatively we derived only lower limits to the downstream magnetic field that have been used to improve constraints on particle acceleration. However, we also found hints of an excess in the 0.5–2 keV SB profile across the relic region. The combination of a possible IC excess in the spectral analysis with the hints of excess in the SB is tantalizing and certainly deserves deeper *Chandra* observations.

ACKNOWLEDGEMENTS

We thank the anonymous referee for the useful comments on the manuscript. We thank Dominique Eckert for his help with the PROFFIT SB analysis. The scientific results reported in this article are based on observations made by the *Chandra* X-ray Observatory. We thank the staff of the GMRT who made these observations possible. GMRT is run by the National Centre for Radio Astrophysics of the Tata Institute of Fundamental Research. AB and GB acknowledge partial support from PRIN-INAF 2014. RK acknowledges support through the DST-INSPIRE Faculty Award.

REFERENCES

Akamatsu H., Kawahara H., 2013, PASJ, 65, 16
Anders E., Grevesse N., 1989, Geochim. Cosmochim. Acta, 53, 197
Bartalucci I., Mazzotta P., Bourdin H., Vikhlinin A., 2014, A&A, 566, A25
Blandford R., Eichler D., 1987, Phys. Rep., 154, 1
Blumenthal G., Gould R., 1970, Rev. Mod. Phys., 42, 237
Bonafede A., Giovannini G., Feretti L., Govoni F., Murgia M., 2009, A&A, 494, 429
Botteon A., Gastaldello F., Brunetti G., Dallacasa D., 2016, MNRAS, 460, L84
Bourdin H., Mazzotta P., Markevitch M., Giacintucci S., Brunetti G., 2013, ApJ, 764, 82
Brüggen M., Bykov A., Ryu D., Röttgering H., 2012, Space Sci. Rev., 166, 187
Brunetti G., Jones T., 2014, Int. J. Mod. Phys. D, 23, 30007
Dasadia S. et al., 2016, ApJ, 820, L20
de Gasperin F., van Weeren R., Brüggen M., Vazza F., Bonafede A., Intema H., 2014, MNRAS, 444, 3130
Donnert J., 2014, MNRAS, 438, 1971

Donnert J., Stroe A., Brunetti G., Hoang D., Roettgering H., 2016, MNRAS, 462, 2014
Eckert D., Molendi S., Paltani S., 2011, A&A, 526, A79
Eckert D., Jauzac M., Vazza F., Owers M., Kneib J.-P., Tchernin C., Intema H., Knowles K., 2016, MNRAS, 461, 1302
Feretti L., Giovannini G., Govoni F., Murgia M., 2012, A&AR, 20, 54
Finoguenov A., Sarazin C., Nakazawa K., Wik D., Clarke T., 2010, ApJ, 715, 1143
Fusco-Femiano R., Dal Fiume D., Feretti L., Giovannini G., Grandi P., Matt G., Molendi S., Santangelo A., 1999, ApJ, 513, L21
Fusco-Femiano R., Orlandini M., Brunetti G., Feretti L., Giovannini G., Grandi P., Setti G., 2004, ApJ, 602, L73
Fusco-Femiano R., Landi R., Orlandini M., 2007, ApJ, 654, L9
Gastaldello F. et al., 2015, ApJ, 800, 139
Guo X., Sironi L., Narayan R., 2014a, ApJ, 794, 153
Guo X., Sironi L., Narayan R., 2014b, ApJ, 797, 47
Kang H., Ryu D., 2016, ApJ, 823, 13
Kang H., Ryu D., Jones T., 2012, ApJ, 756, 97
Kang H., Petrosian V., Ryu D., Jones T., 2014, ApJ, 788, 142
Lindner R. et al., 2014, ApJ, 786, 49
Macario G., Markevitch M., Giacintucci S., Brunetti G., Venturi T., Murray S., 2011, ApJ, 728, 82
Markevitch M., 2006, in Wilson A., ed., ESA SP-604, X-ray Universe 2005. ESA, Noordwijk, p. 723
Markevitch M., Vikhlinin A., 2007, Phys. Rep., 443, 1
Markevitch M., Gonzalez A., David L., Vikhlinin A., Murray S., Forman W., Jones C., Tucker W., 2002, ApJ, 567, L27
Markevitch M., Govoni F., Brunetti G., Jerius D., 2005, ApJ, 627, 733
Marriage T. et al., 2011, ApJ, 737, 61
Menanteau F. et al., 2010, ApJ, 723, 1523
Menanteau F. et al., 2012, ApJ, 748, 7
Million E., Allen S., 2009, MNRAS, 399, 1307
Molnar S., Broadhurst T., 2015, ApJ, 800, 37
Ng K., Dawson W., Wittman D., Jee M., Hughes J., Menanteau F., Sifón C., 2015, MNRAS, 453, 1531
Pinzke A., Oh S., Pfrommer C., 2013, MNRAS, 435, 1061
Planck Collaboration XXIX, 2014, A&A, 571, A29
Press W., Schechter P., 1974, ApJ, 187, 425
Rephaeli Y., Gruber D., 2002, ApJ, 579, 587
Rephaeli Y., Gruber D., Blanco P., 1999, ApJ, 511, L21
Rossetti M., Molendi S., 2004, A&A, 414, L41
Russell H., Sanders J., Fabian A., Baum S., Donahue M., Edge A., McNamara B., O'Dea C., 2010, MNRAS, 406, 1721
Russell H. et al., 2011, MNRAS, 417, L1
Russell H. et al., 2012, MNRAS, 423, 236
Shimwell T., Markevitch M., Brown S., Feretti L., Gaensler B., Johnston-Hollitt M., Lage C., Srinivasan R., 2015, MNRAS, 449, 1486
van Weeren R., Röttgering H., Brüggen M., Hoeft M., 2010, Science, 330, 347
van Weeren R., Brüggen M., Röttgering H., Hoeft M., 2011a, MNRAS, 418, 230
van Weeren R., Hoeft M., Röttgering H., Brüggen M., Intema H., van Velzen S., 2011b, A&A, 528, A38
van Weeren R. et al., 2016, ApJ, 818, 204
Vazza F., Eckert D., Brüggen M., Huber B., 2015, MNRAS, 451, 2198
Vazza F., Brüggen M., Wittor D., Gheller C., Eckert D., Stubbe M., 2016, MNRAS, 459, 70
Vikhlinin A., Markevitch M., Murray S., 2001, ApJ, 551, 160
Wik D., Sarazin C., Finoguenov A., Matsushita K., Nakazawa K., Clarke T., 2009, ApJ, 696, 1700
Wik D., Sarazin C., Finoguenov A., Baumgartner W., Mushotzky R., Okajima T., Tueller J., Clarke T., 2011, ApJ, 727, 119
Zhang C., Yu Q., Lu Y., 2015, ApJ, 813, 129

This paper has been typeset from a TEX/LATEX file prepared by the author.